The Low Detection Rate of Pair–instability Supernovae and the Effect of the Core Carbon Fraction

Koh Takahashi
Argelander-Institut für Astronomie, Universität Bonn, D-53121 Bonn, Germany; ktakahashi@astro.uni-bonn.de

Abstract

The pair-instability supernova (PISN) is a common fate of very massive stars (VMSs). Current theory predicts initial and CO core mass ranges for PISNe of $\sim$140–260 and $\sim$65–120 $M_\odot$, respectively, for stars that are not much affected by the wind mass loss. The corresponding relative event rate between PISNe and core-collapse supernovae is estimated to be $\sim$1% for the present-day initial mass function. However, no confident PISN candidate has been detected so far, despite more than 1000 supernovae being discovered every year. We investigate the evolution of VMSs with various core carbon-to-oxygen ratios for the first time by introducing a multiplication factor $f_{\rm cag} \in [0.1, 1.2]$ to the $^{12}{\rm C}(\alpha, \gamma)^{16}{\rm O}$ reaction rate. We find that a less massive VMS with a high $X({\rm C})/X({\rm O})$ develops shell convection during the core carbon-burning phase, with which the star avoids the pair-creation instability. The second result is the high explodability for a massive VMS; i.e., a star with high $X({\rm C})/X({\rm O})$ explodes with a smaller explosion energy. Consequently, the initial and CO core mass ranges for PISNe are significantly increased. Finally, a PISN with high $X({\rm C})/X({\rm O})$ yields a smaller amount of ^{56}Ni. Therefore, PISNe with high $X({\rm C})/X({\rm O})$ are much rarer and fainter. This result advances the first theory to decrease the PISN event rate by directly shifting the CO core mass range.

Key words: supernovae: general

1. Introduction

The pair-instability supernova (PISN) is known as a common fate of very massive stars (VMSs)[1] that develop massive CO cores during evolution (Barkat et al. 1967; Rakavy et al. 1967). In the massive CO core, the e^- e^+ pair-creation reaction effectively takes place, converting the thermal energy into the rest mass of the $e^- e^+$ pair and softening the pressure. As a consequence, the core becomes hydrodynamically unstable and initiates accelerating core contraction, or core collapse. In the collapsing core, nuclear reactions of carbon, neon, and oxygen burning take place. If the nuclear reactions release enough energy to explode the whole star, then the explosion called PISN takes place in the end. Indeed, hydrodynamical simulations in both 1D (e.g., Heger & Woosley 2002; Umeda & Nomoto 2002; Kozyreva et al. 2014a; Takahashi et al. 2016) and multidimensional (Chatzopoulos et al. 2013; Chen et al. 2014) have resulted in successful explosions, confirming the robustness of the mechanism. The confident understanding of the explosion mechanism provides a strong motivation to search for a PISN explosion in the real universe.

In spite of the robust theoretical prediction, the existence of PISNe has not been observationally confirmed so far. The explosion of a PISN can be observed as a luminous supernova because of the large explosion energy and ^{56}Ni yield (e.g., Kasen et al. 2011), while lower-mass PISNe are expected to be dim (Kasen et al. 2011; Kozyreva et al. 2014a). Therefore, a class of so-called superluminous supernovae (SLSNe), which shows a luminosity 10 or more times larger than that of a standard supernova, is a good candidate to be explained as a PISN event (Gal-Yam et al. 2009; Gal-Yam 2012). However, no currently observed SLSNe match with theoretical predictions, which produce much broader light curves and more red

colors than observations as a result of the intrinsically long diffusion timescale of the large ejecta masses (Dessart et al. 2012, 2013; Kozyreva et al. 2014b, 2016, 2017; Chatzopoulos et al. 2015). Besides, the existence of PISNe in the early universe has not been confirmed yet. Instead of direct detection, PISN explosions in the early universe can be traced by observing surface chemical abundances of metal-poor stars (abundance profiling; Umeda & Nomoto 2002; Nomoto et al. 2013). Although thousands of metal-poor stars have been observed, none of them show agreements with PISN characteristic abundances of low [Na/Mg][2] and high [Ca/Mg] (Takahashi et al. 2018).

Stellar evolution simulations of single nonrotating zero-metallicity VMSs have estimated the mass range of CO cores for PISNe to be $\sim$65–120 $M_\odot$ and the corresponding initial mass range of $\sim$140–260 $M_\odot$ (Heger & Woosley 2002; Takahashi et al. 2016). Assuming the Salpeter initial mass function (IMF) with a slope of $\alpha = 2.35$, a relative number fraction of PISNe to core-collapse supernovae (CCSNe) of $\sim$1% is estimated. The relative event rate between PISNe and CCSNe cannot be directly related to the detection rate because these supernovae will have various luminosities and durations and supernova surveys are magnitude and volume limited. Nevertheless, provided that more than 1000 supernovae are discovered every year by the current supernova surveys (the Latest Supernovae website[3]; Gal-Yam et al. 2013 and references therein), the $\sim$1% relative event rate might be large enough for the PISN detection. Furthermore, the number of detections will be significantly increased after the start of upcoming surveys such as the Zwicky Transient Facility[4]

---

[1] Very massive stars with an initial mass of $>100\,M_\odot$ are conventionally called VMSs (e.g., Vink et al. 2015).

[2] A stellar abundance ratio is indicated by the solar scaled value of $[X/Y] \equiv \log(n_X/n_Y) - \log(n_{X,\odot}/n_{Y,\odot})$, where n_X is the number density of the element X and $n_{X,\odot}$ is the solar value.

[3] http://www.rochesterastronomy.org/supernova.html

[4] http://www.ztf.caltech.edu/

(Bellm 2018) and the Large Synoptic Survey Telescope[5] (Ivezić et al. 2008).

If the PISN confident detection is not achieved even by the upcoming surveys, it will imply that the actual event rate is well below the $\sim1\%$ obtained by the present theory. One important uncertainty related to the event rate estimate is involved in the upper limiting mass for the star formation. If the limiting mass is below the lower end of the PISN mass range, no PISN takes place in the universe. However, the estimated initial mass of $\gtrsim140\,M_\odot$ for a PISN progenitor is not so much massive as regarded as unrealistic. A VMS with an initial mass of $\lesssim320\,M_\odot$ has been observed in star cluster R136 in the Large Magellanic Cloud (Crowther et al. 2010, 2016), and the upper limiting mass for the star formation in the cluster has been estimated to be $\gtrsim200\,M_\odot$ (Schneider et al. 2014), indicating that the formation of a VMS is possible for environments with finite metallicities. Apart from that, star formation in the early universe has been investigated by cosmological ab initio simulations. Because of the absence of efficient coolants in primordial gas clouds, zero-metallicity stars are considered to be born with very massive initial masses of $\sim100\,M_\odot$ (Hirano et al. 2014, 2015; Susa et al. 2014 and references therein).

The other big uncertainties are in the estimate of the initial mass range for PISNe. If the present theory has estimated a lower minimum initial mass for a PISN than the actual value, then it overestimates the event rate because a less massive star is more frequently formed under the present IMF. One of the relevant physics is the strong wind mass loss, and its metallicity dependence is of special importance. Due to the strong wind during both the main sequence and the Wolf–Rayet phases, a solar metallicity VMS of $\lesssim500\,M_\odot$ will not become a PISN (Yusof et al. 2013; Yoshida et al. 2014). As the wind efficiency is reduced, a PISN mass range with the lower metallicity gets close to the zero-metallicity estimate with no mass loss. Provided the big uncertainty of the metallicity dependence, the upper value of $1/3\,Z_\odot$ for the critical metallicity, below which the same PISN mass range as the range for the zero-metallicity model is obtained, is suggested in Langer et al. (2007). Meanwhile, the much higher value of $\gtrsim300\,M_\odot$ is obtained for the lower end of the PISN initial mass range for $\sim1/5\,Z_\odot$ stars in other works (Yoshida & Umeda 2011; Yusof et al. 2013; Yoshida et al. 2014). Apart from the wind mass loss, binary mass transfer can reduce the mass of the primary and increase the mass of the secondary stars. A strong internal magnetic field may suppress the core convection to form a smaller-mass CO core (Petermann et al. 2015), while a strong surface magnetic field may suppress the wind mass loss and thus help to form a massive CO core (Georgy et al. 2017). Also, a CO core may be extended by rotation-induced mixing (Chatzopoulos & Wheeler 2012a; Yoon et al. 2012). All of those mechanisms can shift the initial mass–CO core mass relation to affect the initial mass range for PISNe.

Most of the previous works have implicitly assumed that the CO core mass range of PISNe is well determined, and in fact, less mechanisms have been suggested to shift the CO core mass range for PISNe upward. Multidimensional turbulence that may appear during core collapse and explosion will not affect the hydrodynamical evolution, since the growth time-scale is merely comparable to the timescale of the overall hydrodynamical evolution, and indeed, multidimensional calculations have confirmed the PISN explosion (Chen et al. 2014). A fast rotation of a CO core will regulate the collapsing motion and may affect the CO core mass range for PISNe (cf. Chatzopoulos et al. 2013; Chen 2015). However, a large specific angular momentum of $\gtrsim10^{17}\,\mathrm{cm^2\,s^{-1}}$ is required to affect the PISN explosion (Glatzel et al. 1985). Considering the infrequency of the long gamma-ray burst, the progenitor of which is estimated to have a similar or smaller specific angular momentum of $\sim10^{17}\,\mathrm{cm^2\,s^{-1}}$ to fulfill the constraints of the collapsar model (Woosley 1993; Yoon & Langer 2005; Woosley & Heger 2006), it will be unreasonable to consider that the majority of VMSs form fast-rotating CO cores in the end. An envelope structure of a progenitor is known to affect the PISN explodability. A deflated envelope requires more momentum to be blown off (Kasen et al. 2011; Takahashi et al. 2016). Besides, a progenitor with an inflated envelope has a steeper temperature distribution inside the CO core, and therefore a smaller amount of fuel is available for the nuclear heating with the same maximum central temperature during the explosion (Takahashi et al. 2018). However, the change of the initial mass range by the effect is $\sim10\,M_\odot$ and not so significant.

In this work, we investigate the evolution of VMSs that form CO cores with various carbon-to-oxygen ratios and report the evolutionary consequences that significantly affect the CO core mass range for PISNe for the first time. By introducing a multiplication factor $f_{\mathrm{cag}} \in [0.1, 1.2]$ to the $^{12}\mathrm{C}(\alpha, \gamma)^{16}\mathrm{O}$ reaction rate of Caughlan & Fowler (1988), CO cores with $X(\mathrm{C})/X(\mathrm{O}) \sim 0.15$–$3.1$ are developed. In the next section, we first provide information on the stellar evolution code and a short discussion on the $^{12}\mathrm{C}(\alpha, \gamma)^{16}\mathrm{O}$ reaction rate, then the results of VMS evolution are discussed. For more massive models, the later hydrodynamic evolution is calculated by a 1D hydrodynamic code. The code description is given in the first subsection in Section 3, and the results are discussed in the second subsection. Discussion of the event rate of PISNe and the observational consequences is presented in Section 4. Conclusions are given in the last section.

2. Stellar Evolution Calculation

2.1. Method

The stellar evolution of nonrotating zero-metallicity VMSs is calculated from the zero-age main sequence (ZAMS) until central carbon depletion at least or until iron core formation. An initial mass of a model, M_{ini}, is taken from [120, 460]$\,M_\odot$. The initial composition is determined based on the result of the Big Bang nucleosynthesis of Steigman (2007). Assuming all of the $^2\mathrm{H}$ has burned to form $^3\mathrm{He}$ before the ZAMS stage, mass fractions of $^1\mathrm{H}$, $^3\mathrm{He}$, and $^4\mathrm{He}$ of 0.7599, 8.67×10^{-5}, and 0.2400, respectively, are applied.

Calculations have been done by a stellar evolution code described in Takahashi et al. (2016, 2018), which was originally developed by Japanese researchers (Saio et al. 1988). In order to treat a general massive star evolution, overall physical and numerical descriptions have been improved since then, including the introduction of the wind mass loss and a large reaction network (Yoshida & Umeda 2011), the inertia term and the automatic mesh refinement scheme (Takahashi et al. 2013), and stellar rotation (Takahashi et al. 2014). The
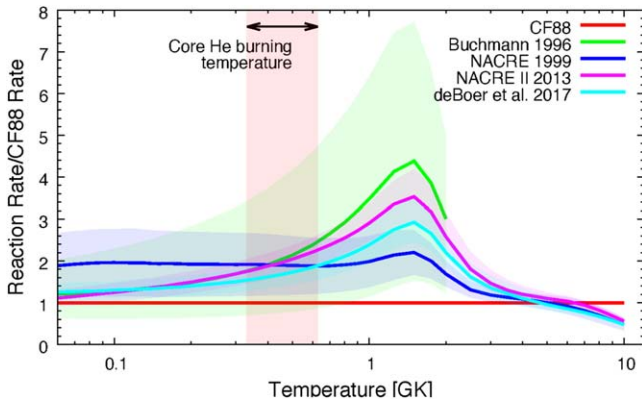

Figure 1. Comparison of the $^{12}C(\alpha, \gamma)^{16}O$ reaction rates in the literature. The ratio between the rates of Buchmann (1996), Angulo et al. (1999; NACRE), Xu et al. (2013; NACRE II), and deBoer et al. (2017) and the rate of Caughlan & Fowler (1988; CF88) are shown with their uncertainties as functions of the temperature. The temperature range relevant for the core helium burning is shaded in red.
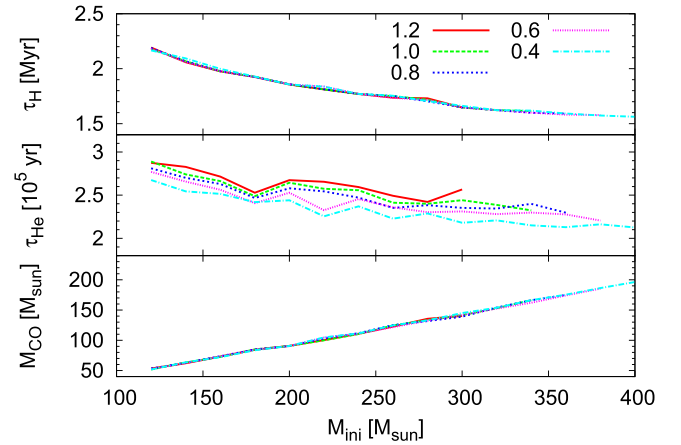

Figure 2. Durations of core hydrogen- (top) and helium-burning (middle) phases and CO core masses (bottom) are shown for models with $f_{cag} = 1.2$ (red solid), 1.0 (green long-dashed), 0.8 (blue short-dashed), 0.6 (magenta dotted), and 0.4 (cyan dashed-dotted).

equation of state in the code includes four species of particles: photon, ion, electron, and positron. Photons are expressed as blackbody radiation, and ions are approximated as the Boltzmann gas. For the electron–positron part, the reaction equilibrium between $e^- e^+$ pair creation and annihilation is assumed, and analytic formulae for general Fermi–Dirac integrals are applied (Blinnikov et al. 1996). The convective overshooting is taken into account for the core hydrogen- and helium-burning phases. An exponentially decaying function is applied with an overshoot parameter of $f_{ov} = 0.015$, with which nonrotating solar metallicity models can account for the wide main sequence (MS) width observed for AB-type stars in open clusters in our galaxy (Maeder & Meynet 1989).

A nuclear reaction network with 49 isotopes, which includes all of the major nuclear reactions affecting the concerned evolution, is incorporated in the stellar calculation. The reaction rates are taken from the current version of JINA REACLIB (Cyburt et al. 2010), except for the $^{12}C(\alpha, \gamma)^{16}O$ reaction.

2.2. The $^{12}C(\alpha, \gamma)^{16}O$ Reaction Rate

Together with the 3α reaction, the $^{12}C(\alpha, \gamma)^{16}O$ is an astrophysically important reaction that determines the $^{12}C/^{16}O$ ratio in the universe. In an He core of a massive star, the reaction takes place with a typical center-of-mass energy of 300 keV, which results in a small cross section of $\sim 2 \times 10^{-17}$ barn. Since the cross section is far below the sensitivity of the current measurements, experimental data that are obtained at the higher energy range have to be extrapolated down to the astrophysically relevant energy range. However, at this higher energy, the cross sections are complicated by the interference from other excited states of ^{16}O. To disentangle the experimental data and conduct a reliable extrapolation, theoretical models such as the R-matrix theory (e.g., Azuma et al. 2010) are required. Due to these complications in both experiment and theory, the reaction rate remains unsettled, despite a number of investigations having been done over the years (cf. deBoer et al. 2017 for a review).

In Figure 1, the $^{12}C(\alpha, \gamma)^{16}O$ reaction rates presented in the literature are compared. In the relevant temperature range for core helium burning in a VMS of 2.1×10^8–4.3×10^8 K, a low value of $f_{cag} \gtrsim 0.8$ is inside the uncertainty of the reaction rate of

Buchmann (1996). On the other hand, the small reaction rate of Caughlan & Fowler (1988) is below the uncertainty ranges of more recent works (Angulo et al. 1999 (NACRE); Xu et al. 2013 (NACRE II); deBoer et al. 2017). Nevertheless, CO cores with various carbon-to-oxygen ratios are calculated by applying a multiplication factor $f_{cag} \in [0.1, 1.2]$ to the reaction rate of $^{12}C(\alpha, \gamma)^{16}O$ of Caughlan & Fowler (1988) in this work. This is because the aim of this work is to display a new route in the massive star evolution that appears when the CO core has a high carbon-to-oxygen ratio. In addition to the small reaction rate, astrophysical origins such as additional mixing may account for the large carbon-to-oxygen ratio. Previous works have shown that the carbon-to-oxygen ratio in a CO core is influenced by convective overshooting (Imbriani et al. 2001) and rotation-induced mixing (Chieffi & Limongi 2013).

The $^{12}C(\alpha, \gamma)^{16}O$ reaction rate has also been inspected by calculating theoretical yields of CCSNe (Weaver & Woosley 1993; Timmes et al. 1995; Woosley & Heger 2007; West et al. 2013; Austin et al. 2017). Because the carbon-to-oxygen ratio affects the electron mole fractions at the end of the stellar evolution, the multiplier of the reaction rate has correlation and anticorrelation to even-Z and odd-Z elemental yields. The same trends have also been found in our calculations of $15\,M_\odot$ models having the converging point at $f_{cag} = 1.2$. Thus, the upper value of $f_{cag} = 1.2$ is the one used in our conventional calculations. Since the resulting carbon-to-oxygen ratio of ~ 0.15 is small, we expect that the evolution applying $f_{cag} = 1.2$ is qualitatively similar to the one from pure oxygen cores. For the same reason, calculations with $f_{cag} = 1.2$ will represent calculations with higher $f_{cag} > 1.2$. This is why we drop calculations with $f_{cag} > 1.2$ from this work, despite the larger reaction rate being more compatible with recent estimates.

2.3. Result

Until core carbon depletion, a zero-metallicity VMS experiences core hydrogen- and helium-burning phases. In Figure 2, the durations of these phases, τ_H and τ_{He}, and resulting CO core mass, M_{CO}, which is defined as the innermost mass coordinate where the helium mass fraction
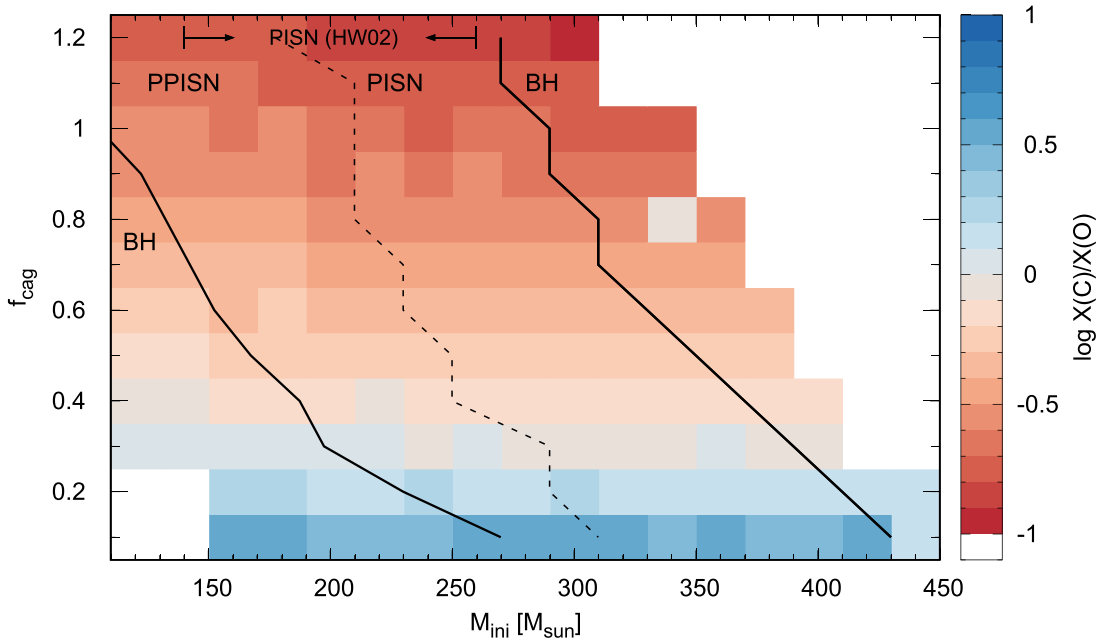
Figure 3. Phase diagram of the zero-metallicity VMSs. The color shows the central $X(C)/X(O)$.

exceeds $X(\text{He}) > 10^{-2}$, are shown as functions of the initial mass, M_{ini}, for selected sequences of f_{cag}. The duration of the hydrogen-burning phase is independent[6] of f_{cag} but depends on the initial mass, because the $^{12}C(\alpha, \gamma)^{16}O$ reaction is irrelevant to the hydrogen burning. On the other hand, models with smaller f_{cag} tend to have slightly shorter helium-burning phases for models with the same initial masses. The CO core mass is again independent from f_{cag}. This is because the size of the convective core is nearly constant during the helium-burning phase.

Hence, the most relevant consequence of applying different f_{cag} is the different carbon-to-oxygen ratio in the same mass CO core. The central $X(C)/X(O)$ measured when the central temperature reaches $\log T_c[\text{K}] = 8.8$ is shown by a color map in Figure 3. The phase space is divided into four regions according to the fate of the model, while the definition of each boundary is explained later. Also, the initial mass range of PISNe indicated by Heger & Woosley (2002) is shown. The color map shows that models with small f_{cag} have high $X(C)/X(O)$. More massive models tend to have less $X(C)/X(O)$; however, the mass dependency is much weaker than the f_{cag} dependency. Thus, models with $f_{cag} = 1.2$ have the lowest $X(C)/X(O) \sim 0.15$, models with $f_{cag} = 0.6$ have intermediate $X(C)/X(O) \sim 0.46$, and models with $f_{cag} = 0.1$ have the highest $X(C)/X(O) \sim 3.1$.

We have found that, due to the high core carbon fraction, less massive models with small f_{cag} develop shell convection during the core carbon-burning phase. The thick solid line passing from $M_{ini} = 110\,M_\odot$ at $f_{cag} = 1.0$ to $M_{ini} = 270\,M_\odot$ at $f_{cag} = 0.1$ in Figure 3 is the upper boundary of the models that

experience this convective shell formation. Figure 4 shows the evolution of convective regions for models of $M_{ini} = 180\,M_\odot$ with different $f_{cag} = 1.2$ (top panel) and 0.3 (bottom panel). No convection develops for the $f_{cag} = 1.2$ case, which has a small $X(C)/X(O)$ of 0.18. On the other hand, a large shell convective region appears at $M_r \gtrsim 10\,M_\odot$ from $\sim 7 \times 10^{-2}$ yr before the calculation end for the $f_{cag} = 0.3$ case, which has a 5.7 times larger ratio of $X(C)/X(O) = 1.04$.

In general, CO core material easily becomes convectively unstable if a certain amount of heating takes place in the shell region. This is because a newly formed CO core in a VMS has nearly homogeneous distributions of entropy and chemical composition as a result of the effective mixing during the previous core helium-burning phase. In addition, an entropy reduction by the neutrino cooling exclusively takes place at the core central region. Therefore, the isentropic structure in the surrounding region remains. Figure 5 shows distributions of the heating and cooling rates and the entropy for the two models when the central temperatures become $\log T_c[\text{K}] = 9.18$. The figure shows that the $f_{cag} = 0.3$ model has a shell region at $M_r \sim 10$–$25\,M_\odot$, where the nuclear heating rate significantly exceeds the neutrino cooling rate. This net heating soon creates a negative entropy gradient and drives shell convection at that region. On the other hand, the nuclear heating rate is only slightly larger than the neutrino cooling rate in the $f_{cag} = 1.2$ model. Except for the carbon-depleted central region, the heatings are solely caused by the $^{12}C + ^{12}C$ reaction. Therefore, the heating rate is proportional to the square of the carbon mass fraction. Given the similar core entropies, the lower heating rate is explained by the lower core carbon fraction. Finally, no convection appears in this model until core collapse sets in.

The evolution of central density and temperature is shown in Figure 6 for selected models. All of the models with $f_{cag} = 1.2$, shown by dashed lines, are nonconvective. For models with $f_{cag} = 0.3$, shown by solid lines, less massive models with $M_{ini} \leqslant 195\,M_\odot$ develop shell convection during the core carbon-burning phase, while more massive models are

---

[6] Actually, tiny differences in τ_H are seen for models with the same initial masses. However, these differences should not have a physical significance but rather a numerical origin. The different f_{cag} affects the evolution of a zero-metallicity VMS during the pre-ZAMS He-burning phase. This difference is enhanced through the evolution of the convective regions around the H-burning core, because the convective evolution is significantly sensitive to any kind of numerical error. Finally, the merging of shell and central convections takes place during the core hydrogen-burning phase in some models, causing the different τ_H.
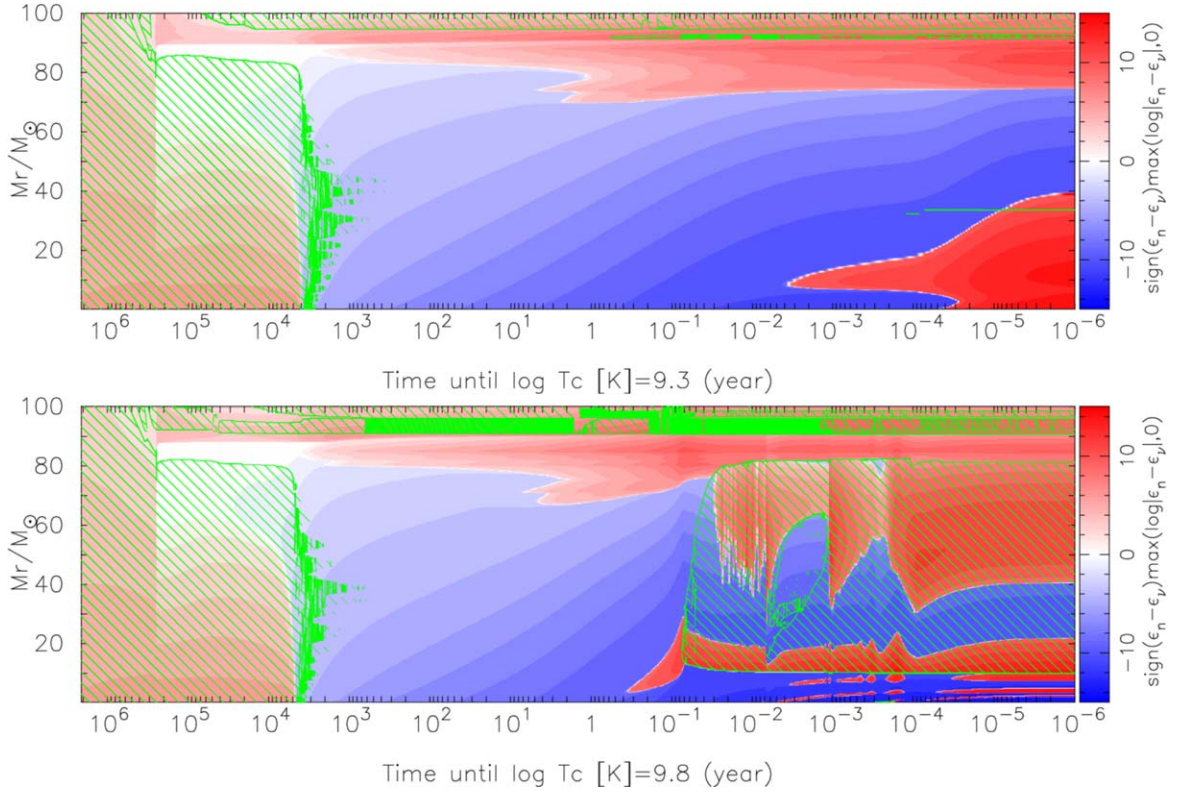
Figure 4. Kippenhahn diagrams of 180 $M_\odot$ models with $f_{cag} = 1.2$ (top) and 0.3 (bottom). The convective evolution is shown from the ZAMS phase until log T_c [K] = 9.3 for the model with $f_{cag} = 1.2$, while that until log T_c [K] = 9.8 is shown for the model with $f_{cag} = 0.3$. Green hatched regions show the convective regions. Colors indicate the net heating (red) or cooling (blue) rates at the region.
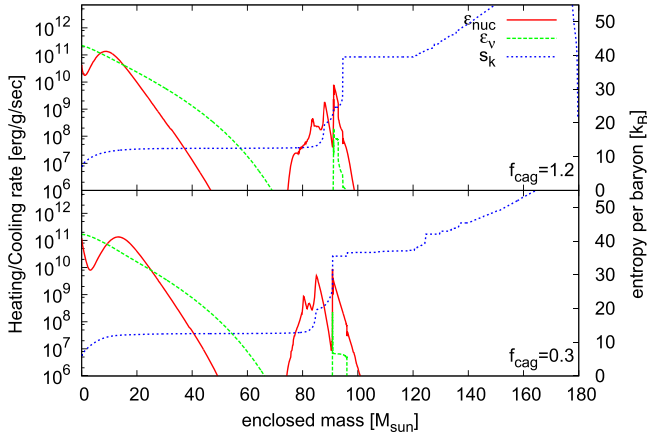

Figure 5. Distributions of nuclear heating rate (red solid), neutrino cooling rate (green dashed), and entropy per baryon (blue dotted) are shown for $M_{ini} = 180\,M_\odot$ models with $f_{cag} = 1.2$ (top) and 0.3 (bottom). Both models have the same central temperatures of log T_c[K] = 9.18.

Figure 6. Central density and temperature evolution. Models with $f_{cag} = 0.3$ are shown by solid lines, while models with $f_{cag} = 1.2$ are shown by dashed lines. Selected initial masses are 140 (red), 180 (green), 240 (blue), and 300 (magenta) $M_\odot$. The boundary of the pair-instability region is shown by the black dotted line.

nonconvective. It is evident that those convective models offset to the lower-entropy side, i.e., the higher density for the same temperature, when the central temperatures reach log T_c[K] ~ 9.2. The branching moments are exactly when the shell convections develop in the cores. Thus, due to the emergence of the shell convective regions, the effective core masses of the convective models are reduced. And, due to the effective neutrino cooling, the central entropies rapidly decrease to match the new core masses. As a consequence, the low-entropy core avoids being affected by the $e^- e^+$ pair-creation instability. No dynamical collapse or energetic
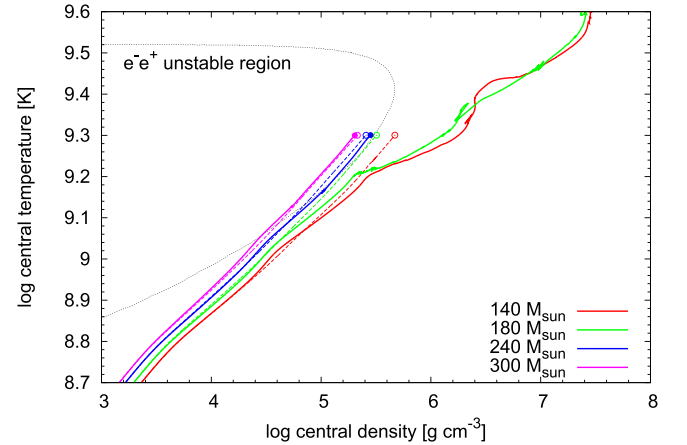
pulsations take place for the convective models. The two convective models shown in Figure 6 form hydrostatic iron cores in the end.

Based on the result, we estimate that the formation of a stellar-mass black hole (BH), instead of an explosion as a PISN, is the fate of convective models. Therefore, the minimum mass to be affected by the $e^- e^+$ pair-creation instability is shifted significantly upward; for example, $M_{ini} > 160\,M_\odot$ for models with $f_{cag} = 0.6$ and $X(C)/X(O) \sim 0.46$ and $M_{ini} > 280\,M_\odot$ for models with $f_{cag} = 0.1$ and $X(C)/X(O) \sim 3.1$. Note that weak pulsations possibly

appear in the outer region of the CO core in reality and are dumped in a time-implicit evolutionary calculation with a long time step. Although the nonlinear coupling with carbon burning may trigger mass ejection and further affect the evolution, this is beyond the scope of this work.

3. Hydrodynamic Calculation

3.1. Method

After the central carbon depletion, nonconvective models with more massive initial masses of $\gtrsim 140\,M_\odot$ are affected by the $e^- e^+$ pair-creation instability. The late hydrodynamic evolution is calculated by a general relativistic hydrodynamic code described in Yamada (1997). A result at $\log T_c$ [K] ~ 9.2 calculated by the stellar evolution calculation is used for the initial structure. Except for the small reaction network with 49 reduced isotopes, which is identical to the evolution calculation in this work, the code settings are the same as in Takahashi et al. (2016, 2018). The equation of state, local neutrino cooling rate, and reaction network are imported from the stellar evolution code (Takahashi et al. 2016).

Chemical mixing and energy transport by convection are not considered in the hydrodynamic code. The code thus has no capability to model the Rayleigh–Taylor instability developing at the core–envelope interface associated with the reverse shock, which may affect the efficiency of the fallback and thus the bounding mass between pulsational PISNe (PPISNe) and PISNe. However, no major instabilities will be developed during the neon- and oxygen-burning phases, and therefore the explosion of PISNe will not be affected by the omission of convection. Chen et al. (2014) showed that only a mild instability grows by oxygen burning in their 2D simulations. This can be understood as the growth time, which may be estimated as $t_{\mathrm{growth}} \sim |N^2|^{-1/2}$, where N is the Brunt–Väisälä frequency, is ~ 10 s at its minimum, and is merely comparable to the timescale of core contraction and expansion around the turning point. Soon after the instability starts to grow, the core expands, and the growth time will be significantly lengthened. Thus, the instability is expected to freeze out for further evolution, which is what is observed in the 2D simulations.

3.2. Result

In Figure 7, the evolution of the total energy, which is defined as $E_{\mathrm{tot}} = \int(\frac{1}{2}U^2 + e^{\mathrm{therm+pair}} - \frac{GM_b}{r})dM_b$, is shown as a function of the central temperature. Here $\rho_b e^{\mathrm{therm+pair}} \equiv \rho_b e^{\mathrm{therm}} + \rho_{\mathrm{pair}}c^2$ is the internal energy density, including the rest mass of the created electron–positron pair (for detailed information, see Takahashi et al. 2016), and U and r are the velocity and radius of the mass shell at the enclosed baryon mass of M_b.

Results of models with $f_{\mathrm{cag}} = 1.2$, shown in the top panel, are essentially the same as those reported in Takahashi et al. (2016). During the contraction, the total energy first increases due to the neon burning that initiates when the central temperature reaches $\log T_c$ [K] ~ 9.3. However, the released energy is small, and the star keeps contracting. Next, oxygen burning sets in after the central temperature reaches $\log T_c$ [K] ~ 9.5, significantly increasing the total energy. The star returns its contracting motion to expansion when enough energy is released by the reaction. On the other hand, when the released energy is insufficient and the central temperature reaches $\log T_c$ [K] ~ 9.75, the next important reaction of the
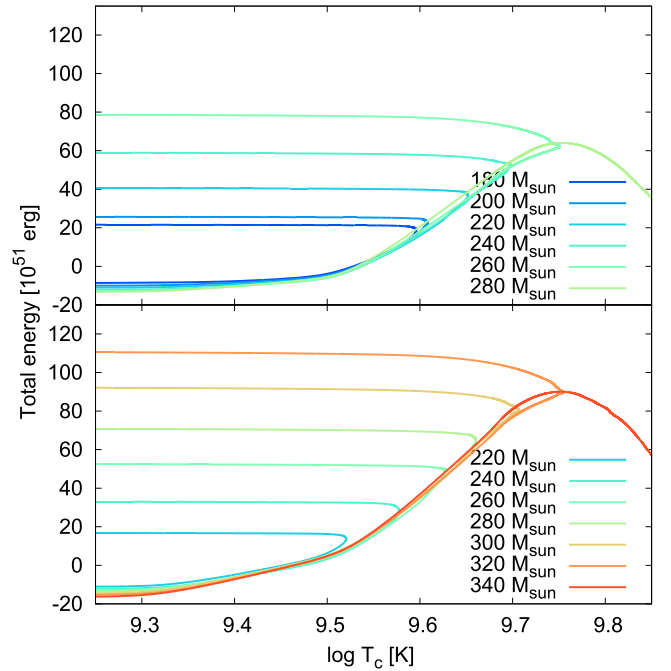

Figure 7. Evolution of the total energy during the explosion. Results of models with $f_{\mathrm{cag}} = 1.2$ and 0.6 are respectively shown by the top and bottom panels.

photodisintegration initiates. Because this reaction converts the internal energy into the rest mass of nuclei, the total energy defined above rapidly decreases. Empirical results obtained by Takahashi et al. (2016) show that the star finally collapses to form a BH if the central temperature exceeds $\log T_c$ [K] ~ 9.8.

The second panel shows the total energy evolution of models with $f_{\mathrm{cag}} = 0.6$. The basic picture discussed for models with $f_{\mathrm{cag}} = 1.2$ is still applicable to other cases with $f_{\mathrm{cag}} < 1.2$; i.e., important temperatures of T_c [K] ~ 9.3, 9.5, and 9.8 divide the hydrodynamic evolution into four phases. On the other hand, the figure also shows that the inclination of energy increase during the neon-burning phase becomes steeper than the case of $f_{\mathrm{cag}} = 1.2$. This is because a model with $f_{\mathrm{cag}} = 0.6$ has a higher core neon fraction. Neon is the prime product of the carbon burning of

$$^{12}\mathrm{C} + {}^{12}\mathrm{C} \rightarrow {}^{20}\mathrm{Ne} + {}^4\mathrm{He}$$
$$^{16}\mathrm{O} + {}^4\mathrm{He} \rightarrow {}^{20}\mathrm{Ne},$$
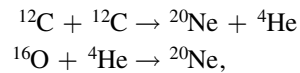
so that the high core carbon fraction before the core carbon-burning phase results in the high core neon fraction after the core carbon depletion. Moreover, the neon burning in the surrounding region has a major contribution for the energy increase even after the central temperature reaches $\log T_c$ [K] ~ 9.5. Therefore, a low-f_{cag} model with the same initial mass has a larger total energy for the same central temperature. As a consequence, a model with lower f_{cag} returns its contracting motion to explosion having a lower central temperature. In other words, models with lower f_{cag} explode more easily than models with higher f_{cag}.

The phase diagram of the fate is again shown in Figure 8 but with the color map showing the total energy 10^4 s after the start of the hydrodynamic calculation. Note that the total energies are shown only for models that have positive total energies after the core collapse. The thick solid line passing from $M_{\mathrm{ini}} = 270\,M_\odot$ at $f_{\mathrm{cag}} = 1.2$ to $M_{\mathrm{ini}} = 430\,M_\odot$ at $f_{\mathrm{cag}} = 0.1$
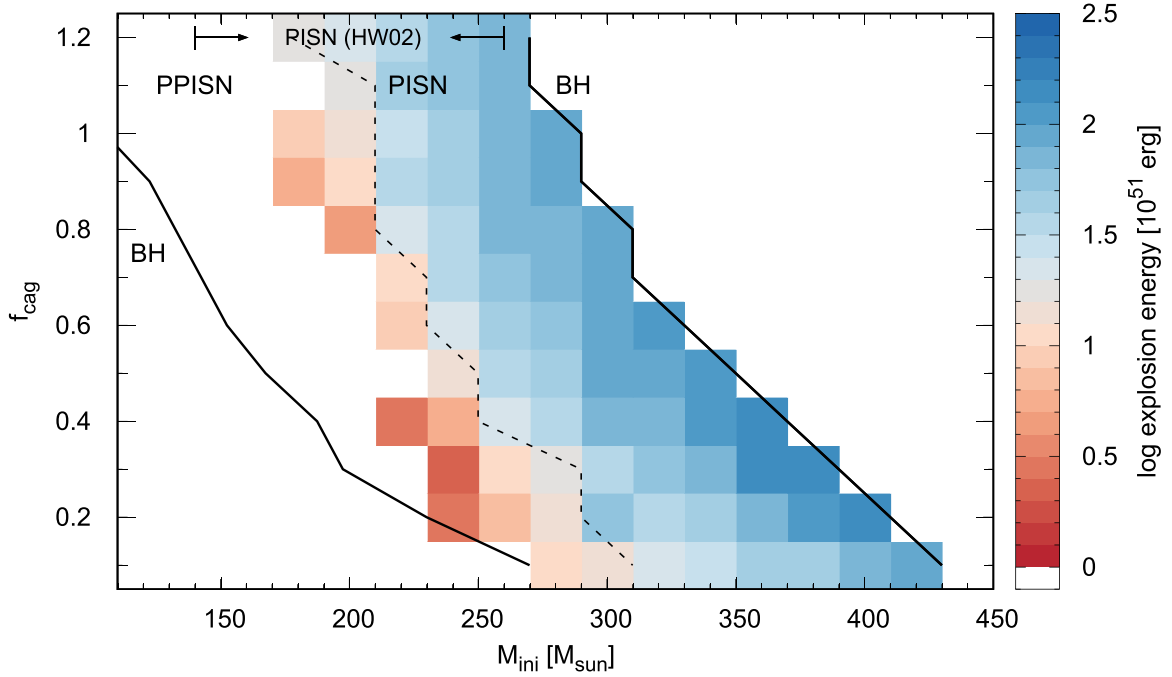
Figure 8. Phase diagram of the zero-metallicity VMSs. For models that have positive total energies after the core collapse, the energies ∼10^4 s after the core collapse are shown by the colors.

shows a boundary between progenitors of PISNe and BH formation. The definition is clear whether the model returns the contracting motion or not.

The boundary between progenitors of PPISNe and PISNe is shown by a dashed line passing from $M_{ini} = 175\,M_\odot$ at $f_{cag} = 1.2$ to $M_{ini} = 310\,M_\odot$ at $f_{cag} = 0.1$. Similar to PISNe, PPISNe are triggered by the $e^- e^+$ pair-creation instability. However, in this case, a central part of the star remains gravitationally bound after the expansion because of the smaller energy injection by the thermonuclear reactions (Woosley et al. 2007; Chatzopoulos & Wheeler 2012b; Chen et al. 2014; Yoshida et al. 2016; Woosley 2017). In this work, an expanding model is considered to be a PPISN if the central mesh of the model restarts contraction after its first expansion 10^4 s from the start of the hydrodynamic calculation. The bounding mass at $f_{cag} = 1.2$ is larger than the results of Heger & Woosley (2002); however, this discrepancy will be well explained as hydrogen-rich envelopes are included in our calculation (Kasen et al. 2011; Takahashi et al. 2016). The central remnant of a PPISN is considered to restart hydrostatic evolution, leading to iron core collapse in the end. Because of the high masses, the fate of PPISN models are determined as BH formation.

The phase diagram clearly shows the strong dependence of the initial mass range of PISNe on the core carbon-to-oxygen ratio. With the highest $f_{cag} = 1.2$, the models have small $X(C)/X(O) \sim 0.15$ and a lower shifted initial mass range of $M_{ini} \in [175, 270]M_\odot$. The initial mass range becomes $M_{ini} \in [240, 320]M_\odot$ for models with the intermediate $f_{cag} = 0.6$ with $X(C)/X(O) \sim 0.46$, and the highest shifted mass range of $M_{ini} \in [310, 430]\,M_\odot$ results from models with the lowest $f_{cag} = 0.1$, which have the largest $X(C)/X(O) \sim 3.1$.

In spite of the very different initial mass ranges, the initial mass dependences of the explosion energy, as well as the elemental yields, are quite similar for models with different f_{cag}.
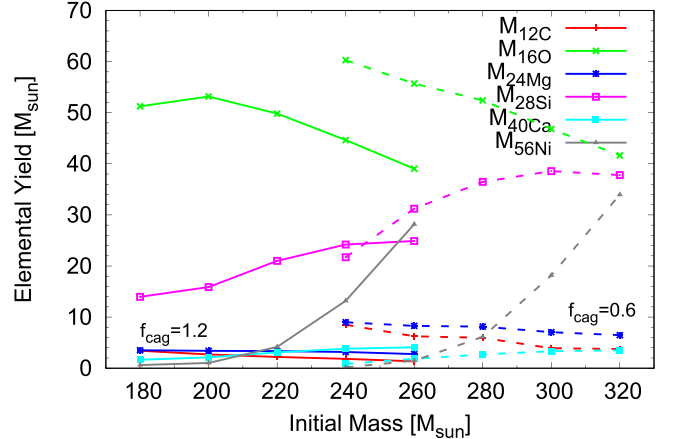

Figure 9. Representative elemental yields (^{12}C in red, ^{16}O in green, ^{24}Mg in blue, ^{28}Si in magenta, ^{40}Ca in cyan, and ^{56}Ni in gray) ejected by a PISN. Results of models with $f_{cag} = 1.2$ and 0.6 are shown by solid and dashed lines, respectively.

The smallest explosion energy keeps ~ 10–30×10^{51} erg for a wide range of f_{cag}, although the initial mass spans a wide range of $M_{ini} \in [175, 310]\,M_\odot$. And, the largest explosion energy increases from $\sim 80 \times 10^{51}$ to $\sim 130 \times 10^{51}$ erg, while the initial mass increases from $260\,M_\odot$ for the $f_{cag} = 1.2$ models to $400\,M_\odot$ for the $f_{cag} = 0.2$ models. The yields of the representative elements are shown in Figure 9 for exploding models with $f_{cag} = 1.2$ and 0.6. The figure clearly shows the similar mass dependencies. As a result, models with the same mass but different f_{cag} can produce totally different explosion energy and elemental yields. For example, $260\,M_\odot$ models have quite different ^{56}Ni yields of $1.48\,M_\odot$ for the model with $f_{cag} = 0.6$ and $28.1\,M_\odot$ for the model with $f_{cag} = 1.2$.

4. Discussion

4.1. PISN Event Rate

In order to demonstrate the impact of a larger mass range of PISN progenitors, we estimate the event rate of PISNe by applying a simple IMF that is characterized by the slope (α) and the upper limiting mass ($M_{\rm up}$) above which no star is born. A typical α for low-redshift PISNe will be the Salpeter value, $\alpha = 2.35$ (however, a small IMF slope of $\alpha \sim 1.90$ was recently obtained for the massive stellar cluster R136; Schneider et al. 2018). A flat value $\alpha = 0$ may be applicable for the IMF of zero-metallicity stars (cf. Hirano et al. 2014). For $M_{\rm up}$, while a low value of $M_{\rm up} < 200 \, M_\odot$ for finite-metallicity stars has been rejected by the population synthesis for the cluster R136 (Schneider et al. 2014), the actual value is quite uncertain for both the low-redshift universe and the early universe (for example, the maximum mass for zero-metallicity stars is estimated as $\lesssim 300 \, M_\odot$ in Susa et al. 2014 and $\lesssim 1000 \, M_\odot$ in Hirano et al. 2015). Therefore, massive values of $> 200 \, M_\odot$ are tested here as a free parameter.

Instead of the absolute value, a relative event rate of PISNe to a rate of CCSNe,

$$\lambda(\alpha, M_{\rm up}, f_{\rm cag}) = \frac{\int_{\min(M_{\rm PISN,min}, M_{\rm up})}^{\min(M_{\rm PISN,max}, M_{\rm up})} M^{-\alpha} dM_{\rm ini}}{\int_{10 M_\odot}^{20 M_\odot} M^{-\alpha} dM_{\rm ini}}, \qquad (1)$$

is calculated, in which the mass range of 10–$20 \, M_\odot$ is assumed for CCSN progenitors. The relative rate λ depends on $f_{\rm cag}$ through $M_{\rm PISN,min}$ and $M_{\rm PISN,max}$, which are the minimum and maximum masses for PISN progenitors, respectively.

Here we assume that the initial mass range for PISN progenitors only depends on $f_{\rm cag}$ and is independent from the metallicity of the star. This can be justified for low-metallicity environments with $Z < 1/3 \, Z_\odot$ (Langer et al. 2007), since a CO core formed in a star with the same initial mass has a nearly metallicity-independent mass unless the efficient wind mass loss significantly reduces the mass of the star. We do not take the effect of the envelope structure into account in this estimate. Whether the envelope of a VMS inflates or not affects the explodability and thus changes the initial mass range of the PISNe (e.g., Takahashi et al. 2018). However, the shift is $\sim 10 \, M_\odot$ and much less effective than the effect of the core carbon fraction considered here.

Also, we do not take the effect of the rotation-induced mixing into consideration. This is because the efficiency of the rotational mixing is highly uncertain. Fast-rotating VMSs in Chatzopoulos & Wheeler (2012a) form extended He cores; as a result, the lower and higher ends of the PISN mass range shift to lower masses. For example, their $95 \, M_\odot$ model with 30% $v_{\rm ZAMS}/\sqrt{1 - \Gamma} \, v_{\rm Kep}$, where $v_{\rm ZAMS}$ is the surface rotation velocity at the ZAMS phase, $v_{\rm Kep} = \sqrt{GM/R}$ is the Kepler velocity, and $\Gamma = L/L_{\rm Edd}$ is the Eddington factor, forms a $90 \, M_\odot$ oxygen core, which has a $40 \, M_\odot$ higher mass than the nonrotating counterpart. On the other hand, a $100 \, M_\odot$ model with 47% $v_{\rm ZAMS}/\sqrt{1 - \Gamma} \, v_{\rm Kep}$ that also has $v_{\rm ZAMS} = 704 \, {\rm km \, s}^{-1}$ and 30% $v_{\rm ZAMS}/v_{\rm Kep}$ in Yoon et al. (2012) develops a $65.81 \, M_\odot$ CO core, and an $85 \, M_\odot$ model with $v_{\rm ZAMS} = 800 \, {\rm km \, s}^{-1}$ in Ekström et al. (2008) forms a $43.92 \, M_\odot$ CO core. They are merely 13.88 and $9.42 \, M_\odot$ larger than their nonrotating counterparts, respectively. Also, in Takahashi et al. (2018), less effective enhancements of 5.80
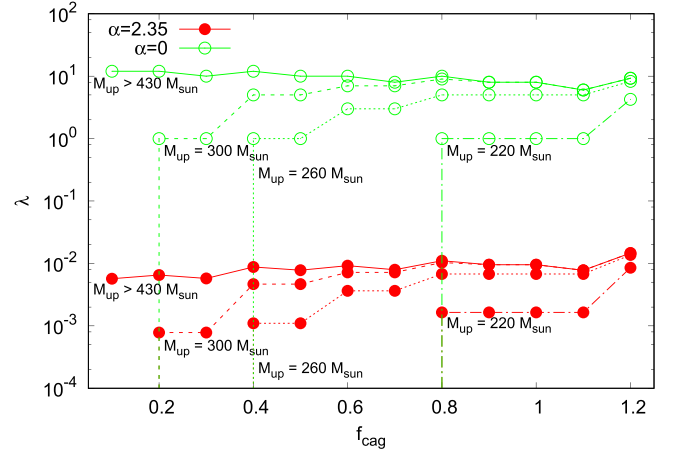

Figure 10. Relative event rate of PISNe. Different colors indicate results with different IMF indexes of $\alpha = 2.35$ (red) and $\alpha = 0$ (green). Results with considerably large $M_{\rm up} > 430 \, M_\odot$ are shown by solid lines, and results with $M_{\rm up} = 300, 260$, and $220 \, M_\odot$ are shown by dashed, dotted, and dashed-dotted lines, respectively.

and $2.29 \, M_\odot$ are obtained in their $100 \, M_\odot$ rotating models of 30% $v_{\rm ZAMS}/v_{\rm Kep}$ with and without the Tayler–Spruit dynamo.

Results are shown in Figure 10. Similar properties are deduced for both results of $\alpha = 2.35$ and 0. If the upper limiting mass in the star formation is considerably large, say, $M_{\rm up} > 430 \, M_\odot$, then the relative event rate is nearly independent from $f_{\rm cag}$. This constant value becomes $\sim 1\%$ for the Salpeter IMF case. Also, the relative rate only slightly depends on $M_{\rm up}$ for the $f_{\rm cag} = 1.2$ case. On the other hand, the relative event rate shows an $M_{\rm up}$ dependency for models with $f_{\rm cag} < 1.2$. In particular, no PISN progenitor is formed under the condition of small $M_{\rm up}$ and small $f_{\rm cag}$. Considering the big uncertainty in the current estimate of $M_{\rm up}$, we conclude that the combination of the small $M_{\rm up}$ and the large carbon-to-oxygen ratio has the potential importance to explain the nondetection of PISNe.

4.2. Observational Consequences

The luminosity of a PISN in the early phase will be powered by diffusion of the thermal energy that is deposited by the shock heating and the radioactive decay of $^{56}{\rm Ni} \rightarrow ^{56}{\rm Co}$. The duration is determined by the diffusion time, which scales as $t_{\rm diff} \sim 2 \times 10^6 \, {\rm s}$ $(M_{\rm ej}/M_\odot)^{3/4} \, (E_{\rm exp}/10^{51} \, {\rm erg})^{-1/4} \, (\kappa/0.4 \, {\rm cm}^2 \, {\rm g}^{-1})^{1/2}$, where $M_{\rm ej}$, $E_{\rm exp}$, and κ are the ejecta mass, explosion energy, and opacity, respectively (Arnett 1980). As the opacity in a PISN is dominated by the electron scattering and thus $\kappa \sim 0.4 \, {\rm cm}^2 \, {\rm g}^{-1}$ (Kasen et al. 2011), the large ejecta mass of a PISN of $\sim 100 \, M_\odot$ results in a long diffusion time of $\gtrsim 200$ days, which characterizes the PISN light curve. The peak luminosity during the diffusion phase will correlate with the explosion energy (cf. Kasen et al. 2011). The late luminosity, which is explained by the $^{56}{\rm Co}$ decay, is estimated as $L_{\rm dec}(t) \sim 1.63 \times 10^{43} \, (M_{^{56}{\rm Co}}/M_\odot) \, \exp(-t/9.60 \times 10^6 \, {\rm s}) \, {\rm erg \, s}^{-1}$ (Arnett 1979), where $M_{^{56}{\rm Co}}$ is the mass of the $^{56}{\rm Co}$, which is originally ejected as $^{56}{\rm Ni}$.

Therefore, a PISN can have a less luminous brightness, if the explosion energy and ejected $^{56}{\rm Ni}$ mass are small. Indeed, the model R175 in Kasen et al. (2011), which is a $175 \, M_\odot$ PISN model producing 21.3×10^{51} erg of the explosion energy and $0.70 \, M_\odot$ of $^{56}{\rm Ni}$, has a peak absolute R-band magnitude of ~ -17 and a fainter decay tail that are rather comparable to a normal SN IIP. Our minimum-mass PISN models for various
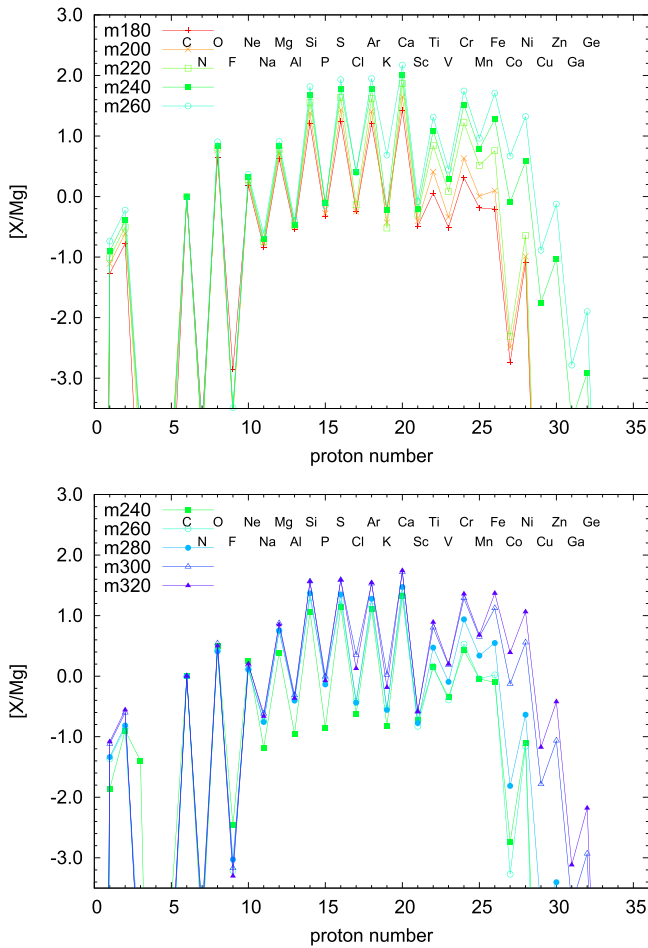
Figure 11. Abundance ratios of PISN explosive yields for models with $f_{cag} = 1.2$ (top) and 0.6 (bottom).

f_{cag} will have similar observational properties to this R175 model, because they also have $\sim 20 \times 10^{51}$ erg of the explosion energies and $\sim 1\,M_\odot$ ^{56}Ni yields. Therefore, the most important observational consequence of the high $X(C)/X(O)$ is the fainter PISN from the same mass progenitors. We expect that the low detectability of PISNe may be explained by the fainter luminosity of the VMS progenitors with higher $X(C)/X(O)$.

Apart from the discussion of low detectability, we discuss some possibilities to constrain the $X(C)/X(O)$ in the real VMSs. For example, the core carbon-to-oxygen ratio can be constrained by determining the relation between the ejecta mass and the explosion energy. This relation can be obtained from the width of the light curve if the explosion energy is determined by another kind of observation, such as line broadening. Similarly, the relation between the ejecta mass and the ^{56}Ni yield also significantly depends on the $X(C)/X(O)$. By observing the late decay tail of the light curve, the ^{56}Ni ejecta mass can be obtained. This will also be a powerful tool to distinguish models with different core carbon-to-oxygen ratios.

On the other hand, no significant distinction is found from PISN yields with different $X(C)/X(O)$, in spite of the big difference in the initial mass ranges. The abundance ratios of PISN explosive yields are shown in Figure 11 for models with $f_{cag} = 0.6$ and 1.2, in which the solar values in Asplund et al. (2009) are used. The low [Na/Mg] and high [Ca/Mg], which characterize the PISN yields from ordinary CCSN yields

(Takahashi et al. 2018), result from both of the sequences. The explosive yields are incapable of discriminating stellar models with different core carbon-to-oxygen ratios.

5. Conclusion

Thanks to the development of automated wide-field surveys, currently more than 1000 supernovae are discovered every year. The large number might be enough for the detection of PISNe, because the relative event rate of $\sim 1\%$ for CCSN events is estimated from the conventional stellar evolution simulations for the Salpeter IMF. However, none of the observed supernovae are known to show characteristic signatures of PISNe, such as the intrinsically red color and broad light curve.

The above estimate of $\sim 1\%$ for the relative event rate of PISNe to CCSNe is based on a conventional estimate for the initial mass range of PISNe of ~ 140–$260\,M_\odot$. Because more massive stars are less frequently formed in the present universe, the event rate of PISNe has possibly been overestimated if the upper and lower ends of the PISN mass range have been underestimated. So far, most estimates of the PISN initial mass range have assumed the well-defined mass range of the CO core for PISNe of ~ 65–$120\,M_\odot$. For example, a strong wind mass loss has been known to affect the PISN event rate by shifting the initial mass range for PISNe upward for VMSs with finite metallicities but without changing the CO core mass range.

In this work, we have investigated the VMS evolution with various core carbon-to-oxygen ratios. By applying a modulation factor of $f_{cag} \in [0.1, 1.2]$ to the reaction rate of ^{12}C(α, γ)^{16}O of Caughlan & Fowler (1988), VMS models developing CO cores with $X(C)/X(O) \sim 0.15$–3.1 have been calculated. The characteristic excited states of the compound nuclei ^{16}O make it challenging to accurately determine the ^{12}C(α, γ)^{16}O reaction rate (deBoer et al. 2017). Although the small reaction rate of Caughlan & Fowler (1988) is below the uncertainty of the most recent estimates (Xu et al. 2013; deBoer et al. 2017), modulation factors of $f_{cag} \gtrsim 0.8$ are compatible with the estimate of Buchmann (1996). Moreover, the high core carbon fraction may result from astrophysical mechanisms such as additional mixing, because the mixing at the convective boundary region during the last part of the core He-burning phase can significantly affect the carbon abundance in the convective core (Imbriani et al. 2001). Thus, it is still interesting to investigate what results from the high carbon fraction in CO cores formed in VMSs.

We have found that VMSs with high core carbon-to-oxygen ratios follow a qualitatively different evolutionary path from conventional models. Less massive models with small f_{cag} avoid the pair-creation instability, since their effective core masses are reduced during the carbon-burning phase by developing shell convection. For example, this takes place for $M_{ini} < 105$, 135, and $155\,M_\odot$ models of the $f_{cag} = 1.0$, 0.8, and 0.6 cases, respectively. Besides, massive exploding models with smaller f_{cag} are found to have higher explodabilities; i.e., stars with a higher core carbon-to-oxygen ratio explode with smaller explosion energies. For example, the explosion energies of the $260\,M_\odot$ models are 73.7, 65.1, and 44.3×10^{51} erg for the $f_{cag} = 1.0$, 0.8, and 0.6 cases, respectively. Consequently, the initial mass range for PISNe increases from $M_{ini} \in [175, 270]\,M_\odot$ for the conservative $f_{cag} = 1.2$ case to $M_{ini} \in [210, 290]$, $M_{ini} \in [210, 310]$, and

$M_{\mathrm{ini}} \in [230, 330]\, M_{\odot}$ for the $f_{\mathrm{cag}} = 1.0$, 0.8, and 0.6 cases, respectively. It has also been found that, as well as the explosion energy, the ^{56}Ni yield significantly decreases with decreasing f_{cag}.

We have estimated the corresponding relative event rate of PISNe to that of CCSNe by integrating a simplified IMF that is characterized by the slope, α, and the upper limiting mass for the star formation, M_{up}. With sufficiently large $M_{\mathrm{up}} > 430\, M_{\odot}$, the relative rate becomes nearly independent from f_{cag}, and a roughly constant value of $\sim 1\%$ is obtained for the Salpeter value of $\alpha = 2.35$. The event rate can be significantly reduced by decreasing M_{up}, and the reduction is more vigorous for models with smaller f_{cag} or higher core carbon-to-oxygen ratios. This result advances the first theory to decrease the PISN event rate not by modifying the initial mass–CO core mass relation but by directly changing the CO core mass range.

Finally, the observational consequences of PISNe with different core carbon-to-oxygen ratios are discussed. Based on the small explosion energies and ^{56}Ni yields, the minimum-mass PISNe for different f_{cag} cases are estimated to have similar luminosities to a normal SN IIP. Therefore, those relatively fainter PISNe may be missed from extensive observations, explaining the low detectability of the PISNe.

ORCID iDs

Koh Takahashi ⬤ https://orcid.org/0000-0002-6705-6303

References

Angulo, C., Arnould, M., Rayet, M., et al. 1999, NuPhA, 656, 3
Arnett, W. D. 1979, ApJL, 230, L37
Arnett, W. D. 1980, ApJ, 237, 541
Asplund, M., Grevesse, N., Sauval, A. J., & Scott, P. 2009, ARA&A, 47, 481
Austin, S. M., West, C., & Heger, A. 2017, ApJL, 839, L9
Azuma, R. E., Uberseder, E., Simpson, E. C., et al. 2010, PhRvC, 81, 045805
Barkat, Z., Rakavy, G., & Sack, N. 1967, PhRvL, 18, 379
Bellm, E. C. 2018, arXiv:1802.10218
Blinnikov, S. I., Dunina-Barkovskaya, N. V., & Nadyozhin, D. K. 1996, ApJS, 106, 171
Buchmann, L. 1996, ApJL, 468, L127
Caughlan, G. R., & Fowler, W. A. 1988, ADNDT, 40, 283
Chatzopoulos, E., van Rossum, D. R., Craig, W. J., et al. 2015, ApJ, 799, 18
Chatzopoulos, E., & Wheeler, J. C. 2012a, ApJ, 748, 42
Chatzopoulos, E., & Wheeler, J. C. 2012b, ApJ, 760, 154
Chatzopoulos, E., Wheeler, J. C., & Couch, S. M. 2013, ApJ, 776, 129
Chen, K.-J. 2015, MPLA, 30, 1530002
Chen, K.-J., Woosley, S., Heger, A., Almgren, A., & Whalen, D. J. 2014, ApJ, 792, 28
Chieffi, A., & Limongi, M. 2013, ApJ, 764, 21

Crowther, P. A., Caballero-Nieves, S. M., Bostroem, K. A., et al. 2016, MNRAS, 458, 624
Crowther, P. A., Schnurr, O., Hirschi, R., et al. 2010, MNRAS, 408, 731
Cyburt, R. H., Amthor, A. M., Ferguson, R., et al. 2010, ApJS, 189, 240
deBoer, R. J., Görres, J., Wiescher, M., et al. 2017, RvMP, 89, 035007
Dessart, L., Hillier, D. J., Waldman, R., Livne, E., & Blondin, S. 2012, MNRAS, 426, L76
Dessart, L., Waldman, R., Livne, E., Hillier, D. J., & Blondin, S. 2013, MNRAS, 428, 3227
Ekström, S., Meynet, G., Chiappini, C., Hirschi, R., & Maeder, A. 2008, A&A, 489, 685
Gal-Yam, A. 2012, Sci, 337, 927
Gal-Yam, A., Mazzali, P., Ofek, E. O., et al. 2009, Natur, 462, 624
Gal-Yam, A., Mazzali, P. A., Manulis, I., & Bishop, D. 2013, PASP, 125, 749
Georgy, C., Meynet, G., Ekström, S., et al. 2017, A&A, 599, L5
Glatzel, W., Fricke, K. J., & El Eid, M. F. 1985, A&A, 149, 413
Heger, A., & Woosley, S. E. 2002, ApJ, 567, 532
Hirano, S., Hosokawa, T., Yoshida, N., et al. 2014, ApJ, 781, 60
Hirano, S., Zhu, N., Yoshida, N., Spergel, D., & Yorke, H. W. 2015, ApJ, 814, 18
Imbriani, G., Limongi, M., Gialanella, L., et al. 2001, ApJ, 558, 903
Ivezić, Ž, Kahn, S. M., Tyson, J. A., et al. 2008, arXiv:0805.2366
Kasen, D., Woosley, S. E., & Heger, A. 2011, ApJ, 734, 102
Kozyreva, A., Blinnikov, S., Langer, N., & Yoon, S.-C. 2014a, A&A, 565, A70
Kozyreva, A., Gilmer, M., Hirschi, R., et al. 2017, MNRAS, 464, 2854
Kozyreva, A., Hirschi, R., Blinnikov, S., & den Hartogh, J. 2016, MNRAS, 459, L21
Kozyreva, A., Yoon, S.-C., & Langer, N. 2014b, A&A, 566, A146
Langer, N., Norman, C. A., de Koter, A., et al. 2007, A&A, 475, L19
Maeder, A., & Meynet, G. 1989, A&A, 210, 155
Nomoto, K., Kobayashi, C., & Tominaga, N. 2013, ARA&A, 51, 457
Petermann, I., Langer, N., Castro, N., & Fossati, L. 2015, A&A, 584, A54
Rakavy, G., Shaviv, G., & Zinamon, Z. 1967, ApJ, 150, 131
Saio, H., Nomoto, K., & Kato, M. 1988, ApJ, 331, 388
Schneider, F. R. N., Izzard, R. G., de Mink, S. E., et al. 2014, ApJ, 780, 117
Schneider, F. R. N., Sana, H., Evans, C. J., et al. 2018, Sci, 359, 69
Steigman, G. 2007, ARNPS, 57, 463
Susa, H., Hasegawa, K., & Tominaga, N. 2014, ApJ, 792, 32
Takahashi, K., Umeda, H., & Yoshida, T. 2014, ApJ, 794, 40
Takahashi, K., Yoshida, T., & Umeda, H. 2013, ApJ, 771, 28
Takahashi, K., Yoshida, T., & Umeda, H. 2018, ApJ, 857, 111
Takahashi, K., Yoshida, T., Umeda, H., Sumiyoshi, K., & Yamada, S. 2016, MNRAS, 456, 1320
Timmes, F. X., Woosley, S. E., & Weaver, T. A. 1995, ApJS, 98, 617
Umeda, H., & Nomoto, K. 2002, ApJ, 565, 385
Vink, J. S., Heger, A., Krumholz, M. R., et al. 2015, HiA, 16, 51
Weaver, T. A., & Woosley, S. E. 1993, PhR, 227, 65
West, C., Heger, A., & Austin, S. M. 2013, ApJ, 769, 2
Woosley, S. E. 1993, ApJ, 405, 273
Woosley, S. E. 2017, ApJ, 836, 244
Woosley, S. E., Blinnikov, S., & Heger, A. 2007, Natur, 450, 390
Woosley, S. E., & Heger, A. 2006, ApJ, 637, 914
Woosley, S. E., & Heger, A. 2007, PhR, 442, 269
Xu, Y., Takahashi, K., Goriely, S., et al. 2013, NuPhA, 918, 61
Yamada, S. 1997, ApJ, 475, 720
Yoon, S.-C., Dierks, A., & Langer, N. 2012, A&A, 542, A113
Yoon, S.-C., & Langer, N. 2005, A&A, 443, 643
Yoshida, T., Okita, S., & Umeda, H. 2014, MNRAS, 438, 3119
Yoshida, T., & Umeda, H. 2011, MNRAS, 412, L78
Yoshida, T., Umeda, H., Maeda, K., & Ishii, T. 2016, MNRAS, 457, 351
Yusof, N., Hirschi, R., Meynet, G., et al. 2013, MNRAS, 433, 1114